Open Ceramics 22 (2025) 100771

Contents lists available at ScienceDirect

Open Ceramics

journal homepage: www.sciencedirect.com/journal/open-ceramics

Novel dual-phase $Ce_{0.8}Gd_{0.2}O_{2-\delta}$ – $Gd_{1-x}Ce_xFe_{1-y}Co_yO_3$ composite oxygen transport membrane

Liudmila Fischer [a,*], Nawar Haddad [b], Ke Ran [c,d], Stefan Baumann [*,a], Doris Sebold [a], Joachim Mayer [c,d], Jürgen Dornseiffer [a], Arian Nijmeijer [b], Olivier Guillon [a,e], Wilhelm A. Meulenberg [a,b]

[a] Institute of Energy Materials and Decives IMD-2, Forschungszentrum Jülich GmbH 52425 Jülich, Germany
[b] Faculty of Science and Technology, Inorganic Membranes, University of Twente 7500 AE Enschede, The Netherlands
[c] Central Facility for Electron Microscopy GFE, RWTH Aachen University 52074 Aachen, Germany
[d] Ernst Ruska-Centre for Microscopy and Spectroscopy with Electrons ER-C, Forschungszentrum Jülich GmbH 52425 Jülich, Germany
[e] Jülich Aachen Research Alliance: JARA-Energy 52425 Jülich, Germany

ARTICLE INFO

Keywords:
Ceria-based composites
Mixed ionic-electronic conductors
Dual phase oxygen transport membrane
Ceramic materials
Microstructure
Doped-ceria
Spinel-type ferrite
Oxygen permeation
Perovskite structure

ABSTRACT

Oxygen Transport Membranes with mixed oxygen ionic-electronic conductivity are investigated for in-situ oxygen separation in various processes such as oxy-combustion or catalytic membrane reactors enabling process intensification. Dual-phase composite membranes are of high interest due to the opportunity selecting thermochemical stable phases conducting oxygen ions and electrons separately. Recently, we reported a novel composite utilizing a donor doped gadolinium ferrite $Gd_{0.85}Ce_{0.15}Fe_{0.75}Co_{0.25}O_3$ as electronic conductor. Here, the composition of this perovskite system is systematically varied and its structural as well as functional properties are investigated. Moreover, the option of a cobalt-free composition is investigated.

1. Introduction

The demand of pure oxygen is gradually increasing from year to year since oxygen is widely exploited for various industrial purposes, such as combustion, oxidation, and as a feed gas for various chemical reactions to name a few. The development transport membranes (OTMs) based on mixed ionic-electronic conducting (MIEC) ceramic materials is a promising alternative to the existing methods like the Linde-process generating pure oxygen by liquefaction of air. These materials are attracting much attention due to their high selectivity for oxygen and their significantly lower energy demand compared to the conventional cryogenic distillation. Thus, OTMs enable oxygen separation from mixed gases and offer an energy efficient solution for different oxygen-intensive industrial sectors [1–3].

Well-known examples of single-phase MIECs are perovskite materials such as $Ba_{0.5}Sr_{0.5}Co_{0.8}Fe_{0.2}O_{3-\delta}$ and $La_{0.6}Sr_{0.4}Co_{0.2}Fe_{0.8}O_{3-\delta}$ with exceptionally high oxygen permeability, what makes them a good OTM material [4–6]. However, the stability at operating conditions is quite an issue for these materials, especially in reducing conditions as well as CO_2- or SO_x-containing atmospheres, which might lead to irreversible reactions, i.e., carbonating reactions [7–9]. In dual-phase materials, on the other hand, it is possible to get a chemically stable composite [1]. Generally, a well-mixed MIEC should provide a high level of ambipolar conductivity and thus high ionic conductivity, as well as considerable electronic conductivity. In dual-phase materials two or more phases coexist and provide a continuous network, contributing to the transport of different charge carriers. As a rule, the ionic conductor serves as a continuous matrix phase and the electronic conductor is uniformly dispersed, but networked throughout the whole membrane volume, facilitating oxygen permeation. This dual-phase membrane concept gives rise to additional opportunities in the selection of materials for OTM, and thus it is an interesting alternative to the known perovskitic cobaltites and ferrites. Additionally, the dual-phase materials typically offer higher stability in acidic and or reducing atmospheres than single-phase ones. However, the oxygen permeation performance could be further improved [10].

---

* Corresponding authors.
E-mail addresses: li.fischer@fz-juelich.de (L. Fischer), s.baumann@fz-juelich.de (S. Baumann).

https://doi.org/10.1016/j.oceram.2025.100771
Received 20 December 2024; Received in revised form 7 March 2025; Accepted 16 March 2025

Previous studies on $Ce_{0.8}Gd_{0.2}O_{2-\delta}$ – $FeCo_2O_4$ (CGO-FCO) dual-phase composites have shown its promise for application as OTM [11–14]. It shows stable oxygen flux even at relatively low driving forces. However, this composite is highly depending on the phase interaction during sintering, resulting in a multi-phase composite, which complicates the microstructure design. The $Gd_{0.85}Ce_{0.15}Fe_{0.75}Co_{0.25}O_3$ (GCFCO) perovskite was found to be a promising alternative to the FCO spinel as an electron-conducting material without any further reaction with the CGO phase during sintering [11]. This donor-doped $GdFeO_3$ perovskite enables sufficient ambipolar conductivity and is expected to be more stable towards reducing atmospheres and/or higher temperatures compared to FCO. Moreover, the CGO-FCO composites show a tendency for kinetic de-mixing in oxygen chemical potential gradients [15–17]. However, there are no further reports about the CGO-GCFCO system.

Therefore, in this paper a more detailed analysis of the CGO-GCFCO membrane as well as the influence of variation of Ce- and Co-substitution in GCFCO is reported. Moreover, cobalt-free variants by omitting or replacing Co with Mn, respectively, are investigated.

2. Experimental

2.1. Samples fabrication

2.1.1. Perovskite phase

$Gd_{1-x}Ce_xFe_{1-y}Co_yO_3$ powders and pellets with various Ce and Co contents according to the investigated compositions shown in Fig. 1 and Table 1 were synthesized by Solid-State Reaction (SSR). Mixtures of the respective oxides (Sigma-Aldrich, Germany) were calcined at 1100 °C for 5 h and subsequently ball milled in ethanol using 5 mm zirconia milling balls.

Disc samples were uniaxially pressed with a diameter of 10 mm and subjected to sintering at 1350 °C for 5 h with heating and cooling rates of 5 K/min and were afterwards ground to a thickness of approximately 0.80 mm in 5 steps using WS FLEX 18C papers of P 400, P 800, P 1200, P 2500 and P 4000 grit. Thin rectangular samples were cut from the polished perovskite pellets for four-probe DC electrical conductivity measurements, using a Struers Secotom-50 machine.

2.1.2. Dual-phase composites

Commercially available $Ce_{0.8}Gd_{0.2}O_{2-\delta}$ (CGO) (Cerpotech, >99 % purity) was used for the composite fabrication. Respective amounts of powders were weighted for CGO-GCFCO compositions with wt. % -ratios 50:50, 60:40, 70:30, 80:20, and 85:15. During 48 h the powder mixtures were ball-milled in ethanol using 5 mm zirconia balls on a roller bench with a speed of 175 rpm. After drying in ambient air at 70 °C for 48 h powder mixtures were pressed with a uniaxial press into disc-shaped membranes with d = 20 mm and sintered at 1200 °C for 5 h in air with the heating rate 5 K min^{-1}. The He Leak test of the sintered pellets showing values close to 10^{-3}- 10^{-6} mbar l/cm^2s confirm gas tightness appropriate for permeation test. After the sintering step, all samples were ground to a diameter of 14.6 mm and 1 mm thickness in 2 steps applying SiC P 800 and P 1200 emery papers (WS FLEX 18C). On both sides of the discs a porous $La_{0.58}Sr_{0.4}Co_{0.2}Fe_{0.8}O_{3-\delta}$ (LSCF) catalytic activation layer with a thickness of ~5 μm was applied via a screen-printing technique and calcined in air at 1100 °C for 5 h with heating and cooling rates of 5 K/min.

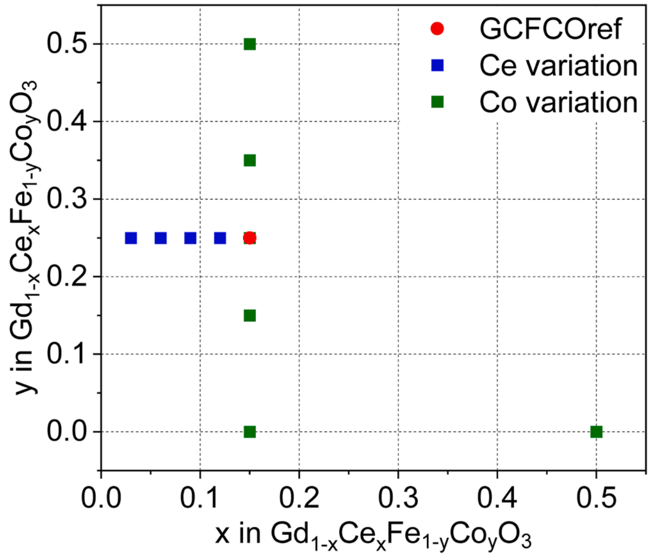

Fig. 1. Roadmap of the investigated A- and B-sites variation in the perovskite phase $Gd_{1-x}Ce_xFe_{1-y}Co_yO_3$.

Table 1
Prepared compositions of the perovskite phase $Gd_{1-x}Ce_xFe_{1-y}M_yO_3$, M = Co, Mn.

abbreviation	x	y	abbreviation	x	y
GCFCO_REFf	0.15	0.25	GC15FO	0.15	0
GCFMnO	0.15	0.25	GC50FO	0.50	0
Ce-Variation			**Co-Variation**		
GC3FCO	0.03	0.25	GCFC15O	0.15	0.15
GC6FCO	0.06	0.25	GCFC25O	0.15	0.25
GC9FCO	0.09	0.25	GCFC35O	0.15	0.35
GC12FCO	0.12	0.25	GCFC50O	0.15	0.5

2.2. Characterization methods

2.2.1. Crystal structure

The X-ray diffraction (XRD) diffractometer D4 ENDEAVOR (Bruker, Germany) is exploited for crystal structure determination. The diffraction angle 2θ is in the range from 10° to 80°, with increments of 0.02° 2θ and 0.75 s of measurement time per step. Measured data is analysed with the help of the program package X'Pert HighScore (PANalytical B.V., version 3.0.5) software. Crystal structure analysis and associated phase quantifications were carried out by Rietveld refinement using the software Profex (Version 4.2.2). The errors of each fit are calculated individually and given in brackets in Table 2–4.

2.2.2. Microscopy

To obtain material morphology Scanning Electron Microscopy (SEM) and Energy Dispersive X-ray Spectroscopy (EDXS) were used. SEM images were taken with a Zeiss Ultra 55 and a Zeiss Supra 50 VP1 (Carl Zeiss NTS GmbH, German) SEM at different magnifications. The electronic conductivity of the samples was enhanced by sputter deposition of platinum prior to the SEM measurement.

Further image analysis-based method was conducted via ImageJ software on all composite samples including ~1000 grains utilizing so-called isodata threshold method [18], which helped to estimate the average grain size of all phases as well as area fraction of pores. However, the limited number of characterized grains/pores might induce large inaccuracy in the grain size and pore size calculations.

For Transmission Electron Microscopy (TEM) lamellas were cut from sintered composite pellets by Focused Ion Beam (FIB) using an FEI Strata 400 system with a gallium ion beam. Further thinning and cleaning was done by using an argon ion beam in a Fischione Nanomill 1040 at beam energies of 900 eV and 500 eV. The FEI Titan G2 80–200 ChemiSTEM microscope equipped with an XFEG and a probe Cs corrector was used in order to obtain high-resolution high-angle annular dark-field (HAADF) images and EDXS chemical mapping [19].

2.2.3. Electrical conductivity characterization

Temperature dependent electrical conductivity measurements were conducted on the $Gd_{1-x}Ce_xFe_{1-y}Co_yO_3$ compositions listed in Table 1 and performed with an experimental set up shown in Fig. 2.

Table 2
Fraction (F) and lattice parameter (a, b, c) of the phases in 60 wt%CGO - 40wt%GCFCO composites after sintering quantified by Rietveld refinement.

			CGO, Fd3m			GC_xFC_yO, Pnma				
	Ce	Co	F, wt.%	F vol.%	$a = b = c$, Å	F, wt.%	F, vol.%	Lattice parameter, Å		
	x	y						a	b	c
GCFCO	0.15	0.25	60.62	61.55	5.4222	39.38	38.45	5.329	5.592	7.638
GC15FO	0.15	0	56.10	57.06	5.4201	43.90	42.94	5.354	5.603	7.672
GC50FO	0.5	0	68.86	69.69	5.4190	31.14	30.30	5.357	5.595	7.635
GC3FCO	0.03	0.25	60.47	61.41	5.4228	39.53	38.60	5.325	5.583	7.627
GC6FCO	0.06	0.25	62.88	63.79	5.4229	37.12	36.21	5.326	5.587	7.630
GC9FCO	0.09	0.25	62.53	63.45	5.4228	37.47	36.55	5.326	5.589	7.632
GC12FCO	0.12	0.25	62.42	63.34	5.4219	37.58	36.66	5.327	5.589	7.630
GCFC15O	0.15	0.15	64.54	65.60	5.4216	35.40	34.40	5.340	5.605	7.657
GCFC25O	0.15	0.25	64.11	65.01	5.4217	35.89	34.99	5.340	5.605	7.657
GCFC35O	0.15	0.35	62.65	63.56	5.4219	37.35	36.44	5.532	5.589	7.625
GCFC50O	0.15	0.50	62.00	62.92	5.4244	38.00	37.08	5.306	5.569	7.60

Table 3
Lattice parameter and fraction (F) of the phases after quantification by Rietveld refinement analyses of (100-z) wt.%CGO - z wt.% $Gd_{0.85}Ce_{0.15}Fe_{0.75}Co_{0.25}O_3$ composites and CGO singe phase sintered at 1200 °C for 5 h.

	CGO, *Fd3m*		GCFCO, *Pnma*			
GCFCO, %	F, wt.%	$a = b = c$, Å	F wt.%	a, Å	b, Å	c, Å
0	100.0	5.4246 [3]	–	–	–	–
15	87.73 [1]	5.4231 [4]	12.27 [2]	5.3302 [8]	5.5938 [6]	7.6356 [4]
20	81.87 [6]	5.4224 [5]	18.13 [8]	5.3302 [2]	5.5988 [4]	7.6358 [1]
30	72.61 [8]	5.4226 [1]	27.39 [2]	5.3302 [5]	5.5972 [8]	7.6344 [8]
40	60.89 [5]	5.4222 [2]	39.11 [5]	5.3298 [6]	5.6035 [2]	7.6407 [2]
50	51.03 [2]	5.4207 [8]	48.97 [4]	5.3273 [1]	5.5907 [5]	7.6340 [2]

For each $Gd_{1-x}Ce_xFe_{1-y}Co_yO_3$ composition, the electrical conductivity was measured at four different temperatures (500, 600, 700 and 800 °C) under air atmosphere. Rectangular samples were cut out of the sintered discs. As electrodes, gold wires (0.25 mm in diameter, Alfa Aesar 99.99 %) were attached around the outer ends of the samples to provide current and two additional gold wires were wrapped around the samples at a remote distance from the sample end to collect the voltage signal (Fig. 2). In order to improve the contact between the gold wires and the surface of the sample, gold paste was used. The dimensions of rectangular samples measurements, i.e., length L, width W, thickness H and distance between the inner voltage electrodes D are approximately 12, 6, 0.80 and 6 mm, respectively, and individually measured for each sample.

2.2.4. Oxygen permeation measurements

All composite materials were subjected to oxygen permeation experiments. The experimental setup consisted of vertical quartz glass housing, where the membrane pellets were sealed with two gold rings with an inner diameter of 13 mm. The separation of the oxygen from ambient air fed with 250 $ml_N\ min^{-1}$ was performed in a temperature range between 650 °C and 1000 °C. As a sweep gas argon was used with 50 $ml_N\ min^{-1}$ flow rate using mass flow controllers (Bronkhorst, Germany). The mass spectrometer (Omnistar, Pfeiffer Vacuum GmbH, Germany) detected concentrations of oxygen and nitrogen in the permeate gas, i.e., oxygen enriched argon. With help of measured nitrogen concentration, air leakage through either membrane or the sealing was calculated according to Eq. (1).

$$j_{O_2} = F_{Ar}\left(\frac{X_{O_2} - \frac{1}{4}X_{N_2}}{1 - X_{O_2} - X_{N_2}}\right)\frac{1}{A_{mem}} \tag{1}$$

Here F_{Ar} is the argon flow rate, i.e., 50 $ml_N\ min^{-1}$, X_{O2} and X_{N2} the oxygen and nitrogen concentration in the permeate gas, respectively, and open membrane area is A_{mem}=1.33 mm^2. The factor $\frac{1}{4}$ reflects the O_2/N_2 ratio in the air feed assuming that the leak is not gas selective.

Since the oxygen partial pressure in the permeate gas is temperature dependent, the driving force of the permeation rate is not constant during the measurement. Additionally, the sample thickness deviation after the grinding process was ±8 % from the target thickness of 1 mm. Consequently, the driving force normalized permeation rate, also referred to as permeance, was normalized to the reference thickness of L_0 = 1 mm and was calculated assuming Wagner behaviour, i.e. bulk diffusion is the dominating transport process and surface exchange limitations as well as concentration polarizations in the gas phases are neglected, using Eq. (2).

Table 4
Lattice parameter and fraction (F) of the phases after quantification by Rietveld refinement analyses of 60CGO - 40FCO and 60CGO - $40Gd_{1-x}Ce_xFe_{1-y}Co_yO_3$ composites after permeation measurement.

	CGO, Fm***3m***		**FCO,** Fd***3m***		Co_3O_4**, *Fd3m***		GC_xFC_yO**, *Pnma***				**CoO *Fm3m***
	F, wt.%	$a = b = c$, Å	F wt.%	$a = b = c$, Å	F, wt.%	$a = b = c$, Å	F, wt.%	Lattice parameter, Å			F, wt.%
								a	b	c	
60CGO - 40FCO											
Prior	52.1[6]	5.418[4]	22.3[4]	8.29[6]	16.61[6]	8.13[4]	9.0[1]	5.34[0]	5.608[5]	7.64[4]	–
feed	42.18[1]	5.418[6]	28.1[6]	8.30[5]	20.62[6]	8.15[2]	6.43[9]	5.33[8]	5.61[6]	7.65[1]	1.28[1]
sweep	60.98[3]	5.419[2]	15.9[9]	8.36[6]	7.89[3]	8.10[6]	9.42[4]	5.34[1]	5.61[6]	7.65[5]	0.43[1]
60CGO - 40GCFCO											
Prior	60.89[2]	5.4222[7]	–	–	–	–	39.11[4]	5.33[4]	5.603[1]	7.64[2]	–
feed	60.77[5]	5.4222[4]	–	–	–	–	39.23[8]	5.33[5]	5.5935[3]	7.63[1]	–
sweep	60.17[2]	5.4221[2]	–	–	–	–	39.83[2]	5.33[5]	5.599[4]	7.63[5]	–

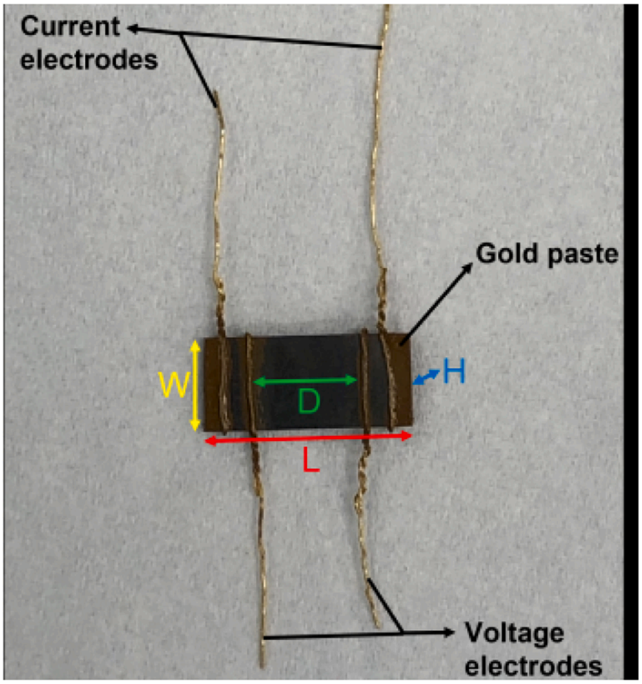

Fig. 2. Experimental set up for the conductivity measurement of $Gd_{1-x}Ce_xFe_{1-y}Co_yO_3$ pellets.

$$Permeance = \frac{j_{O_2}}{ln\frac{p'_{O_2}}{p''_{O_2}}}\frac{L_{mem}}{L_0} \tag{2}$$

Here, p'_{O_2} and p''_{O_2} are the oxygen partial pressures in the retentate and permeate gas, respectively, and L_{mem} is the actual membrane thickness. The overall experimental error is assumed to be ±10 %.

3. Results and discussion

3.1. $Gd_{1-x}Ce_xFe_{1-y}Co_yO_3$ perovskites

3.1.1. Phase composition

XRD patterns of $Gd_{1-x}Ce_xFe_{1-y}Co_yO_3$ compositions according to Table 1 and Fig. 1 are presented in Fig. 3. The formation of orthorhombic perovskite, $GdFeO_3$, is confirmed in all investigated samples. In addition, the presence of a minor ceria phase with cubic fluorite structure, i.e. $(Ce,Gd)O_2$, can be observed in most specimens, which was quantified by Rietveld refinement, Fig. 4. It is well known that the perovskite lattice can easily tolerate 5 mol % sub-stoichiometry on the A-site, so that no third phase containing B-site elements compensating the missing A-site elements in the perovskite lattice can be observed. Therefore, the majority of the samples are considered as single phase, i.e., 95 - 100 wt. % perovskite.

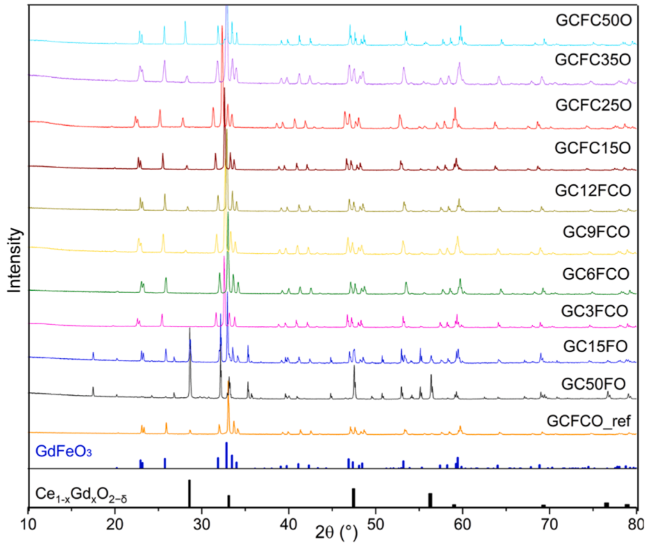

Fig. 3. XRD patterns of the perovskite $Gd_{1-x}Ce_xFe_{1-y}Co_yO_3$ after sintering at 1350 °C prepared by Solid-state reaction.

From Fig. 4 it can be concluded that the solubility of Ce in the $GdFeO_3$ is below 9 mol % while between 12 and 15 mol % Ce-substitution the amount of the ceria phase is relatively constant at 3–4 wt %. The phase composition is not sensitive to B-site variation except for GCFC50O with 50 mol.% of Co on the B-site, which shows a very high fraction, i.e., 14 wt. %, of ceria. Interestingly, still no third phase can be detected. The presence of the Gd-Ce fluorite phase is observed in almost all perovskites. However, this phase acts as ionic conductor and, thus, no negative effect on the composites' MIEC properties is expected.

3.1.2. Electrical conductivity

The temperature dependent electrical conductivity of the perovskite materials is shown in Fig. 5. The Ce^{4+} substituting Gd^{3+} acts as a donor and, thus, electronic conductivity is introduced [17,20–22]. However, in studied perovskites the Ce fraction on A-site between 0.03 to 0.12 does not have much influence on the conductivity, indicating that this mechanism has a minor effect. In contrast, the impact of the Co substitution on the B-site is very pronounced with a clear trend of increasing conductivity when substitution level is increased from 15 to 50 mol %. The influence of aliovalent cobalt on the electrical properties of perovskites is well known. However, the reference composition, $Gd_{0.85}Ce_{0.15}Fe_{0.75}Co_{0.25}O_3$, showed negligible oxygen permeation, thus ambipolar conductivity, in a previous investigation [16]. Therefore, it can be concluded that the GCFCO system is a predominant electronic conductor. All the Arrhenius-type electrical conductivity curves appear rather parallel, i.e. show similar activation energies in the range of 55-70 kJ·mol^{-1}, suggesting that electronic conduction in the different $Gd_{1-x}Ce_xFe_{1-y}Co_yO_3$ compositions occurs according to a similar mechanism, which typically is the small polaron hopping in perovskitic ferrites and cobaltites [23,24].

The conductivity difference between 25 and 35 mol % B-site substitution is not very significant and, thus, this range seems to be a good compromise between stability (secondary phase formation) and electrical conductivity.

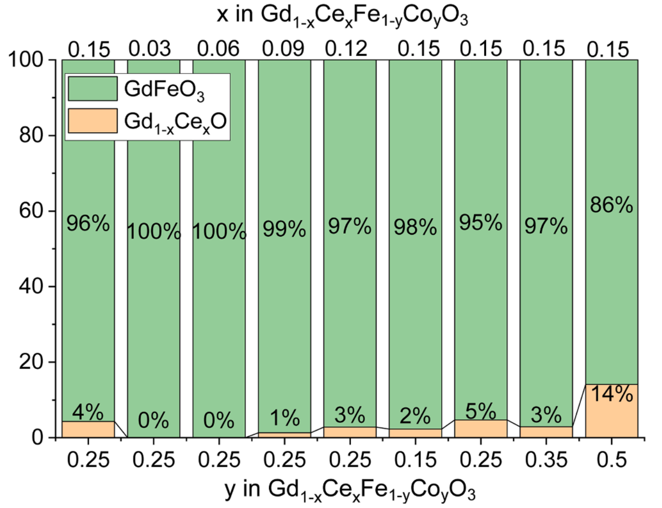

Fig. 4. Phase fractions detected in $Gd_{1-x}Ce_xFe_{1-y}Co_yO_3$ after sintering at 1350 °C for 5 h quantified by Rietveld refinement.

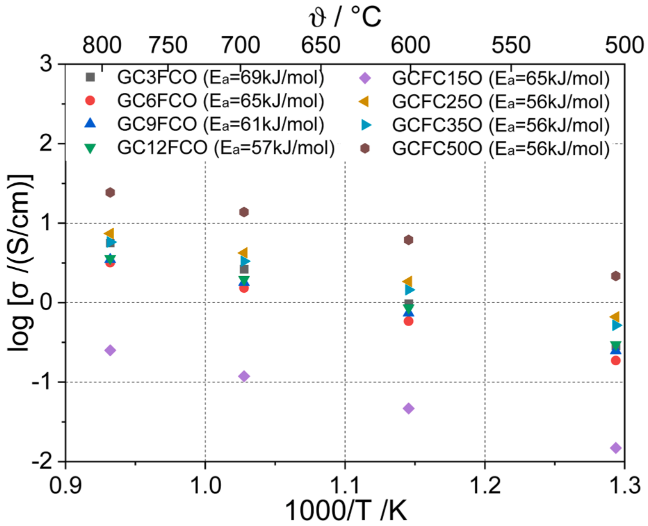

Fig. 5. Arrhenius plot of the electrical conductivity of different $Gd_{1-x}Ce_xFe_{1-y}Co_yO_3$ perovskites.

It should be noted that the limited amount of ceria, potentially doped with Gd, in the perovskite powder is not detrimental for the use in dual phase OTM, where the GCFCO is intentionally mixed with CGO anyways. Moreover, the A-site non-stoichiometry might have even a positive defect-chemical effect on ionic or electronic conductivities by introducing oxygen vacancies or electronic defects, respectively [25]. This aspect requires further specific investigation, which is beyond the scope of this study.

3.2. 60:40 wt% CGO- $Gd_{1-x}Ce_xFe_{1-y}Co_yO_3$ composites

3.2.1. Phase composition

Compositional and structural characterization is carried out for pellets with nominal composition of 60 wt.% CGO- 40 wt. % GCFCO. XRD patterns confirmed the presence of two phases: a cubic fluorite phase, i.e., ceria, and perovskite structure, $GdFeO_3$-based. There is no significant change in the weight fraction from nominal 60:40 ratio, Table 2, which confirms no phase interaction during sintering for all variations.

The resulting oxygen permeance of these surface activated membranes are plotted as a function of the cerium and cobalt fraction in $Gd_{1-x}Ce_xFe_{1-y}Co_yO_3$ at 750, 850 and 1000 °C in Fig. 6. All permeances are mostly within the estimated experimental error of ± 10 %. Along the investigated A-site substitution range between 0.03 and 0.15 (Fig. 6a), there is a slight increase in the oxygen permeance with the maximum for $x = 0.15$ at all temperatures corresponding with a slight decrease in E_a. The B-site substitution improves the permeance until $y = 0.25$ (Fig. 6b), further increase in Co substitution does not have any significant effect. The E_a of all composites with either A-site or B-site substitution vary in the range of 71- 86 kJ·mol^{-1}, which agrees well with that of the ionic conductivity of CGO reported in literature ($E_{a\ CGO20}$=61–80 kJ/mol [26, 27]). It can be concluded that the ionic transport is rate limiting in the investigated composites with relatively high fraction of electronic conductor, i.e. GCFCO. Consequently, only very low σ_e observed for $y = 0.15$ leads to lower permeance, while an increased σ_e obtained by high B-site substitution $y \geq 0.25$ does not affect ambipolar conductivity and, thus, permeance significantly. This might change systematically if the phase mixture is shifted towards higher ceria amounts in the composite, Reducing the GCFCO content would lead to lower electronic conductance and at a certain point the ambipolar conductivity is dominated by the electronic conductivity. In such case an increased B-site substitution might lead to increased permeance.

3.3. CGO-GCFCO_ref composite

3.3.1. Microstructure

Since the reference perovskite phase $Gd_{0.85}Ce_{0.15}Fe_{0.75}Co_{0.25}O_3$ with $x = 0.15$, $y = 0.25$ revealed a good compromise between stability and functionality, compositional and structural characterization is carried out for pellets with varying nominal composition of (100-z) wt.% CGO- z wt. % GCFCO, where $15 \leq z \leq 50$. XRD patterns in Fig. 7 confirmed the presence of a cubic fluorite and perovskite phase, i.e. ceria and $GdFeO_3$, respectively. In contrast to previously investigated dual-phase CGO-FCO composites [11], there is no phase interaction during the sintering process, thus indeed a dual-phase membrane material is achieved for all

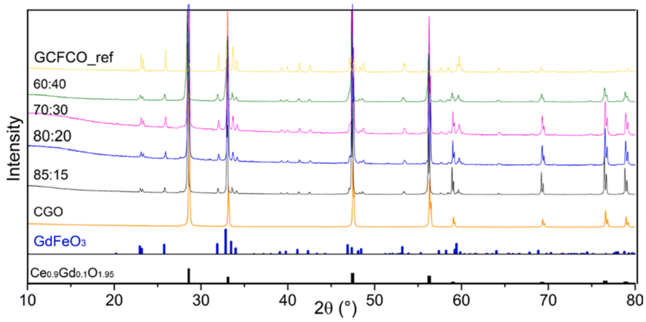

Fig. 7. The XRD patterns of CGO-GCFCO_ref composite materials with varying wt-ratio sintered at 1200 °C for 5 h and single-phase CGO and GCFCO as well as peak positions of phases.

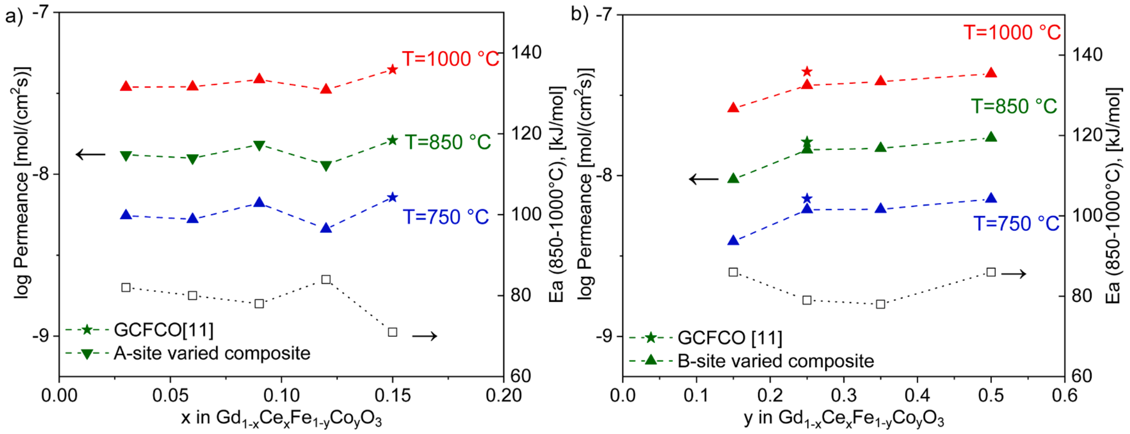

Fig. 6. Permeance of 60CGO-GCFCO composites at 750, 850 and 1000 °C with a) A-site variation at $y = 0.25$, b) B-site variation at $x = 0.15$.

ratios.

Further Rietveld refinement quantified the weight fractions of each phase as shown in Table 3. The resulting amount of fluorite is about 1.5 ± 1 wt.% more in each sintered composite compared to the nominal CGO content in the initial powder mixture, which is likely due to the excess of ceria in the pre-synthesized perovskite.

SEM analysis confirmed the presence of two phases in CGO-GCFCO_ref composites: fluorite CGO (light grains), and perovskite GCFCO (dark grey grains), without any other detectable phase. The grains are closely packed and uniformly distributed, exemplarily shown for 60:40 wt.%-ratio in Fig. 8. The microstructure analysis of both surface and cross-section images via ImageJ software reveals the homogeneous distribution of the phases with a mean grain size of 0.44 ± 0.05 μm and 0.35± 0.05 of GCFCO and CGO respectively. In general, such homogeneous and small grain size is favourable in composites with random phase distribution relying on percolation of pathways for different charge carriers, i.e. electrons/holes and oxygen ions/vacancies, by maximizing contiguity of both phases [22]. A tailored texturing of the microstructure might further increase performance, but this is not in the scope of this investigation.

The grain boundaries between CGO and GCFCO are shown in the HAADF image for 85CGO-15GCFCO_ref composite in Fig. 9. All the grains are closely packed without any intergranular structures. Around the grain boundaries the crystal structures of each grain are resolved down to the atomic scale, indicating no significant segregations or defects along the grain boundaries, which again confirms that no phase interactions occurred.

Fig. 10 contains an HAADF image of a CGO—CGO grain boundary in the 85CGO-15GCFCO_ref composite. Both fluorite grains, G1 and G2, are randomly oriented. G1 appears brighter in the image as well as in the EDS element maps most likely because it is closer to a zone axis compared to G2. As indicated by the white arrow, intensity profiles across the grain boundary were extracted and plotted in Fig. 10b.

The significant enrichment of the gadolinium together with the slight enrichment of the migrated iron and cobalt was detected, while the cerium is significantly depleted between neighbouring CGO grains. A slight depletion in oxygen, i.e., segregation of oxygen vacancies, can be observed. This is in agreement with literature about pure Gd-doped ceria [11–13,28], where excess of Gd^{3+} and depletion of oxygen ions in the grain boundary core appears, what can be also considered as an accumulation of the oxygen vacancies [29–31]. Additionally, an excess of electrons near the grain boundary can be expected, as reported by Lei *et al.* [32].

3.3.2. Oxygen permeation

Fig. 11a shows the temperature-dependent oxygen permeance of the CGO-GCFCO_ref composite with various wt.%-ratios of the two phases. As expected, the permeance decreases with decreasing temperature. Conversely, an increasing CGO content in the composite leads to increasing permeance (Fig. 11b), reaching a broad maximum at 60:40 wt % ratio. Around that maximum the E_a is between 71 and 75 kJ/mol corresponding to that of the ionic conductivity of CGO, which, thus, is likely the rate limiting process. At higher CGO amounts E_a raises up to 108 kJ/mol.

3.3.3. Kinetic stability

SEM-analysis of CGO-GCFCO_ref samples was performed prior and after permeation measurements and compared to previously reported CGO-FCO membranes [11]. The samples were not coated with LSCF surface layers in order to enable post-test surface analysis.

Back scattered electron SEM images (Fig. 12left) reveal the pronounced de-mixing, i.e. motion of the FCO spinel phase (dark) to the air side. Due to the applied oxygen chemical potential gradient (air vs Ar) an opposite chemical potential gradient for the cations results, which act as driving force for cation diffusion. As reported previously [20], the FCO phase is a very good cation conductor compared to CGO and, thus, kinetic de-mixing is observed already after relatively short time at elevated temperatures (approx. 48 h). The post-test Rietveld refinement of XRD measurements confirms the results from the SEM investigation. Table 4 lists the phase fractions of the dual-phase composites after permeation measurement on both sides, which is graphically represented in Fig. 13. The fraction of CGO significantly decreases and increases at the feed and sweep side, respectively. FCO and Co_3O_4 show the opposite trend, while the GCFCO fraction in the CGO-FCO composite is reduced at the feed side probably because it is covered with large FCO grains growing out of the surface. In addition, a minor amount of CoO appears after the measurement.

This phase segregation has a negative effect on the percolation in the dual-phase material in the bulk as well as the amount of the triple phase boundaries at the surface, both negatively affecting oxygen permeation performance. In extreme case, the surface might be completely covered by FCO and the oxygen permeation would break down. The spinel phases, in contrast to GCFCO perovskites, are quite mobile and, thus, CGO-FCO composites are prone to kinetic demixing while such effects cannot be observed in the CGO-GCFCO system, Fig. 12right, revealing the superior stability of this material system.

3.4. Co-free composites

Cobalt is considered to be a critical element in the European Union for several reasons, e.g. toxicity, import dependency, and ethical aspects in the mining practice. The B-site doping in perovskites provides the opportunity to tailor its conductivity, so that optimisation with aliovalent metal cations other than cobalt can be done.

Two approaches are followed. First, cobalt is replaced by iron with varying donor cerium-substitution at the A-site, i.e. $Gd_{1-x}Ce_xFeO_3$ with x = 0.15 and 0.5 (GC15FO and GC50FO), leading to a lesser number of cations in the perovskite potentially further increasing stability. Another typical transition metal in conductive perovskites is manganese. Research on solid oxide cells (SOC) shows that lanthanum strontium manganite (LSM) is a standard cathode material where manganese plays a key role in electronic conduction. Drawbacks in SOC operation are

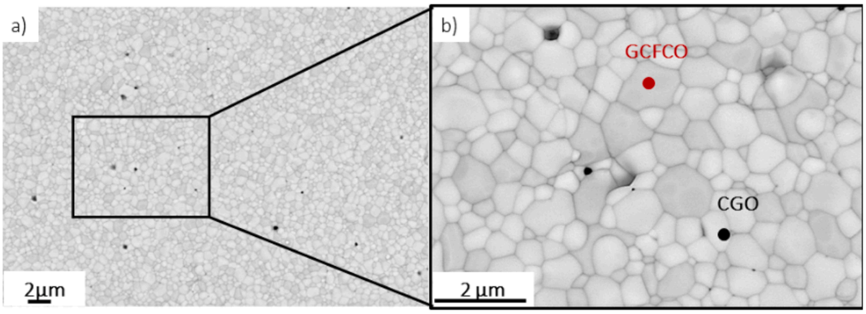

Fig. 8. SEM image of 60CGO-GCFCO_ref sintered at 1200 °C for 5 h a) overview; b) detail with marked fluorite (light) and perovskite (dark) grains.

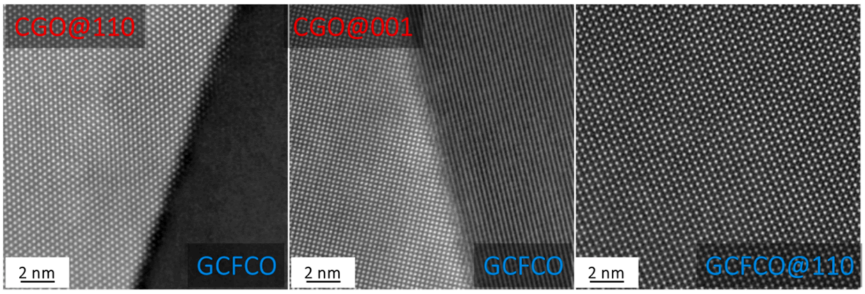

Fig. 9. HAADF image of grain boundaries between phases in the 85CGO-15GCFCO system (a) CGO[110] - GFO; (b) CGO[001] -GFO; (c) GFO [110] of perovskite grain.

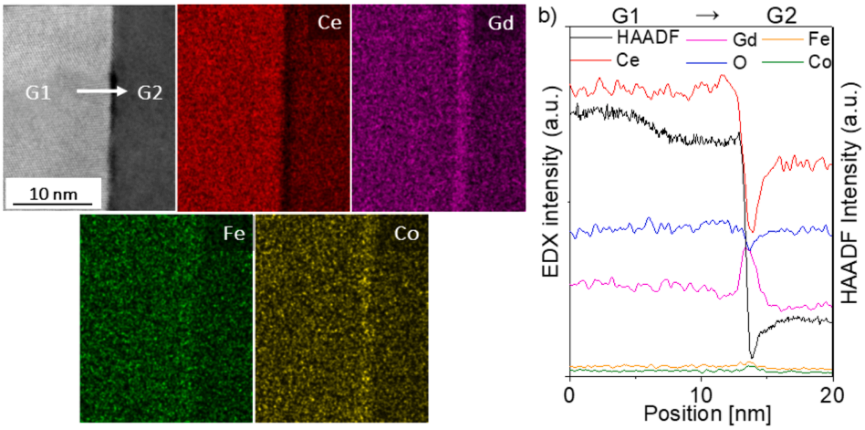

Fig. 10. EDXS analysis of the grain boundaries CGO—CGO in 85CGO-15GCFCO_ref a) The simultaneously acquired HAADF image and EDXS element mapping from Ce L, Gd L, Fe K, Co K, and O K peak. b) Line scans between two fluorite grains marked as G1 and G2 based on the elemental maps.

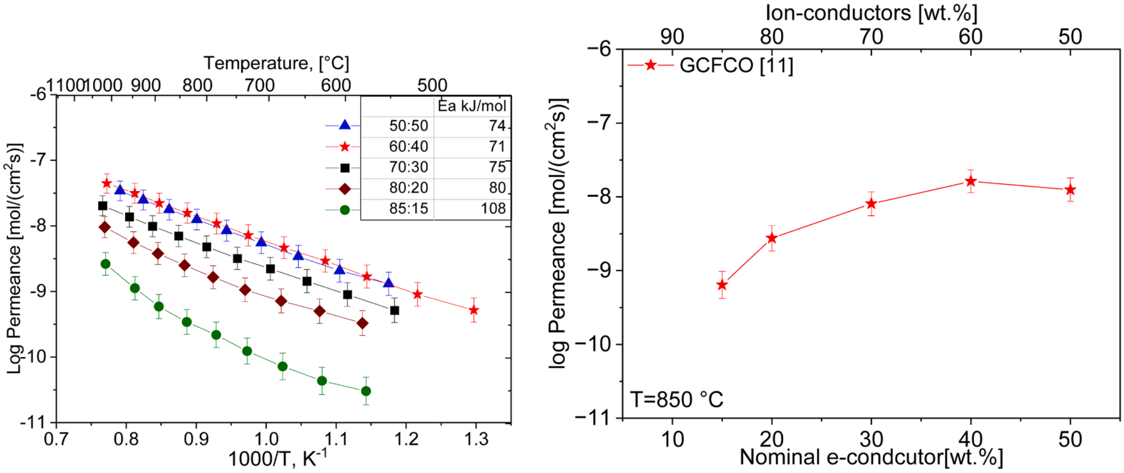

Fig. 11. left: Arrhenius-type plots of oxygen permeance for different CGO-GCFCO_ref wt-% ratios, right: Permeance dependence on phase composition.

related to limited ionic conductivity and stability issues according to chromia poisoning or $SrZrO_3$ formation when mixed with zirconia, which are less relevant for the use in ceria-based MIEC composites [33, 34]. On the other hand, the stability versus reduction of $La_{0.9}Sr_{0.1}MnO_3$ for instance is reasonably good, i.e. decomposition at 900 °C occurs at very low oxygen partial pressures of around 10^{-17} bar [35].

Therefore, Co was replaced by Mn keeping the same substitution level as the reference perovskite, i.e. $Gd_{0.85}Ce_{0.15}Fe_{0.75}Mn_{0.25}O_3$ (GCFMnO), in order to check functionality of this concept. Further investigation on varying composition and stability has to follow in future works.

3.4.1. *Phase composition of Co-free perovskites*

Both GCFO materials did not show phase purity after synthesis and have additional phases such as Gd-doped ceria, magnetite Fe_3O_4, and $Gd_3Fe_5O_{12}$, as shown in Table 5 and Fig. 14. The latter gadolinium iron garnet, has a cubic structure, and is in the space group *Ia3d*, with respect to the Fe-Co phase diagram [36]. It is also likely that this phase contains traces of cerium cations on the A-site. Such garnet phase was also found in former iron rich CGO-FCO composites, i.e. CGO-Fe_2CoO_4 [28] and CGO-Fe_2O_3 [12] showing lower conductivity compared to the perovskite-like structure.

The GCFMnO perovskite shows 90 % phase purity. Compared to the

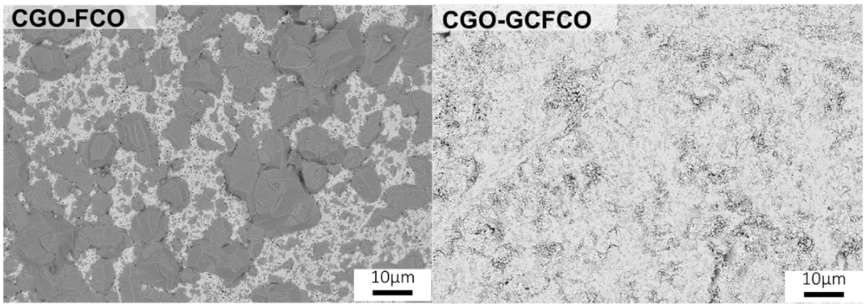

Fig. 12. BSE-SEM images of the surfaces at high p_{O2} side after permeation measurement in CGO-FCO (left) and CGO-GCFCO_ref (right) composites with wt-ratio of 60:40.

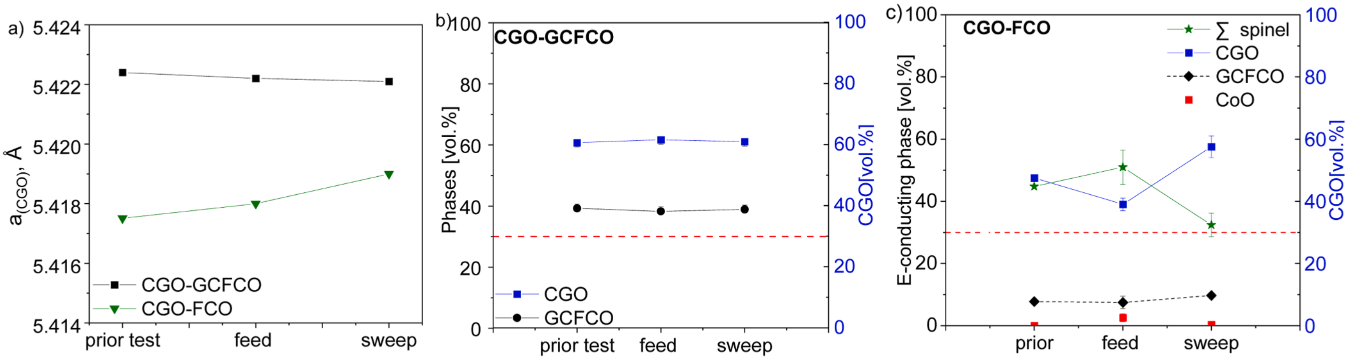

Fig. 13. The phase fractions before and after permeation measurement in CGO-GCFCO and CGO-FCO composites with ratio 60:40.

Table 5
Lattice parameter and fraction (F) of the phases after quantification by Rietveld refinement analyses of the Co-free perovskites.

	CGO, *Fd3m*		$Gd_3Fe_5O_{12}$, *Ia3d*		GC_xFC_yO, *Pnma*			
	F, wt.%	a = b = c, Å	F, wt.%	a = b = c, Å	F wt.%	a, Å	b, Å	c, Å
GCFCO_ref	60.62 [3]	5.4222[6]	–	–	39.38[6]	5.329[1]	5.592[3]	7.638[6]
GC15CFO	55.92[4]	5.4202[5]	0.80 [7]	12.564[4]	43.90[3]	5.354[9]	5.603[1]	7.672[8]
GC50CFO	65.46[6]	5.4198[1]	12.34[3]	12.471[1]	22.20[5]	5.357[4]	5.595[5]	7.635[3]
GCFMnO	62.73[1]	5.4198[4]			36.87[4]	5.346[6]	5.562[5]	7.638[1]

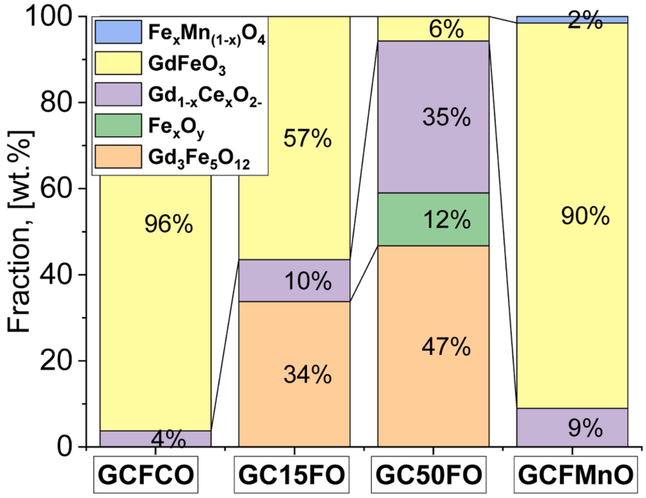

Fig. 14. The phase composition of the cobalt-added and cobalt-free perovskite phases compared to the GCFCO_ref.

reference perovskite GCFCO the CGO impurity is increased from 4 wt% to 9 wt%. in addition, about 2 wt.% of Fe-Mn-rich spinel phase can be detected.

3.4.2. Functional properties

Fig. 15 shows the temperature dependent oxygen permeance of the Co-free composites compared to the standard CGO-GCFCO ref with nominal wt.ratio of 60:40. Both GCFO-based composites show low performance with high activation energy most probably due to the complex phase mixture providing only limited electronic conductivity [11]. CGO-GCFMnO comes closer to that of CGO-GCFCOref with a comparable activation energy, which is in the range of that of ionic conductivity of CGO and, thus, it can be concluded that the permeance is limited by the ionic conductivity. The electronic conductivity of the GCFMnO phase is compared to the B-site-doped GCFCO-series in Fig. 15b. It is in a reasonable range, but a bit lower compared to the reference GCFC25O at temperatures above 700 °C. Since the substitution level of Mn y = 0.25 is arbitrary chosen, there is a good chance to further improve its properties.

4. Conclusions

The perovskite phase in novel $Ce_{0.8}Gd_{0.2}O_{2-\delta}$ -$Gd_{1-x}Ce_xFe_{1-y}Co_yO_3$ MIEC composites was being investigated.

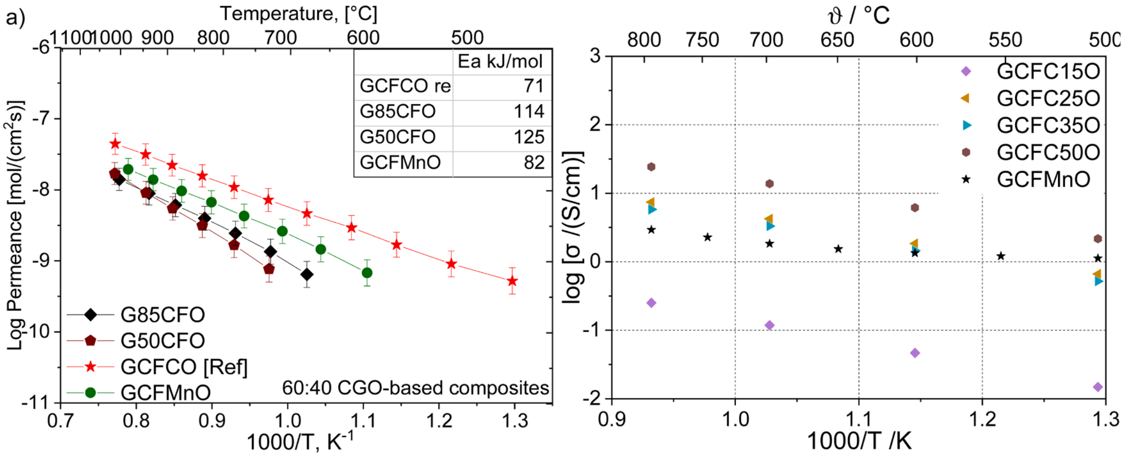

Fig. 15. a) Arrhenius-type plots of composites' permeances with 60:40 wt-ratio (solid lines are a guide to the eye) b) the conductivities of the pure perovskite phases.

The substitution concentration of the donor ion Ce^{4+} in GCFCO is below 9 mol%. In case of higher substitution level up to 15 mol% a secondary ceria phase probably doped with gadolinium is formed. However, this secondary phase is not detrimental for application in composites with CGO. The B-site substitution in GCFCO plays a key role for electrical conductivity. 25–35 mol% of cobalt at the B-site turned out to be a reasonable substitution level. In that case, the oxygen permeance in composites with 60:40 wt%-ratio of CGO:GCFCO is limited by the ionic conductivity of CGO revealing that the electronic conductivity of GCFCO is sufficient to form an effective MIEC composite. In consequence, its oxygen permeance is comparable to other ceria-based MIEC composites reported in literature [1]. At lower substitution, i.e. 15 mol %, the conductivity drops significantly. On the other hand, phase purity suffers from higher substitution, i.e. 50 mol%. Therefore, $Gd_{0.85}Ce_{0.15}Fe_{0.75}Co_{0.25}O_3$ is a promising electron conducting perovskite composition for the use in MIEC composites for OTM applications. But, the GCFCO phase provides higher stability in particular towards reductive atmospheres. There is no phase change at higher temperatures and the kinetic de-mixing phenomenon – reported for CGO-FCO –cannot be observed.

Moreover, the perovskite phase enables a cobalt-free composite by replacing cobalt with manganese. This novel CGO-GCFMnO composite needs further investigation towards permeance optimization as well as stability investigation.

CRediT authorship contribution statement

Liudmila Fischer: Writing – original draft, Investigation. **Nawar Haddad:** Writing – review & editing, Investigation. **Ke Ran:** Writing – review & editing, Investigation. **Stefan Baumann:** Writing – review & editing, Project administration, Funding acquisition, Conceptualization. **Doris Sebold:** Writing – review & editing, Investigation. **Joachim Mayer:** Writing – review & editing, Supervision, Funding acquisition. **Jürgen Dornseiffer:** Writing – review & editing, Supervision. **Arian Nijmeijer:** Writing – review & editing, Supervision. **Olivier Guillon:** Writing – review & editing, Supervision. **Wilhelm A. Meulenberg:** Writing – review & editing, Supervision.

References

[1] R. Kiebach, S. Pirou, L. Martinez Aguilera, A.B. Haugen, A. Kaiser, P.V. Hendriksen, M. Balaguer, J. García-Fayos, J.M. Serra, F. Schulze-Küppers, et al., A review on dual-phase oxygen transport membranes: from fundamentals to commercial deployment, J. Mater. Chem. A 10 (2022) 2152–2195.

[2] W. Bai, J. Feng, C. Luo, P. Zhang, H. Wang, Y. Yang, Y. Zhao, H. Fan, A comprehensive review on oxygen transport membranes: development history, current status, and future directions, Int. J. Hydrogen. Energy 46 (2021) 36257–36290.

[3] G. Chen, A. Feldhoff, A. Weidenkaff, C. Li, S. Liu, X. Zhu, J. Sunarso, K. Huang, X. Y. Wu, A.F. Ghoniem, et al., Roadmap for sustainable mixed ionic-electronic conducting membranes, Adv. Funct. Mater. 32 (2022).

[4] S. Baumann, J.M. Serra, M.P. Lobera, S. Escolástico, F. Schulze-Küppers, W. A. Meulenberg, Ultrahigh oxygen permeation flux through supported Ba0.5Sr0.5Co0.8Fe0.2O3−δ membranes, J. Memb. Sci. 377 (2011) 198–205.

[5] J.M. Serra, J. Garcia-Fayos, S. Baumann, F. Schulze-Küppers, W.A. Meulenberg, Oxygen permeation through tape-cast asymmetric all-La0.6Sr0.4Co0.2Fe0.8O3−δ membranes, J. Memb. Sci. 447 (2013) 297–305.

[6] J. Zhao, Y. Pang, C. Su, S. Jiang, L. Ge, Toward high performance mixed ionic and electronic conducting perovskite-based oxygen permeable membranes: an overview of strategies and rationales, Energy Fuels. 37 (2023) 7042–7061.

[7] J. Gao, L. Li, Z. Yin, J. Zhang, S. Lu, X. Tan, Poisoning effect of SO_2 on the oxygen permeation behavior of $La_{0.6}Sr_{0.4}Co_{0.2}Fe_{0.8}O_{3-\delta}$ perovskite hollow fiber membranes, J. Memb. Sci. 455 (2014) 341–348.

[8] D. Matras, A. Vamvakeros, S.D.M. Jacques, V. Middelkoop, G. Vaughan, M. Agote Aran, R.J. Cernik, A.M. Beale, In situ X-ray diffraction computed tomography studies examining the thermal and chemical stabilities of working $Ba_{0.5}Sr_{0.5}Co_{0.8}Fe_{0.2}O_{3-\delta}$ membranes during oxidative coupling of methane, Phys. Chem. Chem. Phys. 22 (2020) 18964–18975.

[9] T. Ramirez-Reina, J.L. Santos, N. García-Moncada, S. Ivanova, J.A. Odriozola, Development of robust mixed-conducting membranes with high permeability and stability, in: P. Granger, V.I. Parvulescu, V.I. Parvulescu, W. Prellier (Eds.), Perovskites and Related Mixed Oxides, Wiley, 2016, pp. 719–738.

[10] J.H. Joo, K.S. Yun, C.Y. Yoo, J.H. Yu, Novel oxygen transport membranes with tunable segmented structures, J. Mater. Chem. A 2 (2014) 8174–8178.

[11] L. Fischer, K. Neuhaus, C. Schmidt, K. Ran, P. Behr, S. Baumann, J. Mayer, W. A. Meulenberg, Phase formation and performance of solid state reactive sintered $Ce_{0.8}Gd_{0.2}O_{2-\delta}$ -$FeCo_2O_4$ composites, J. Mater. Chem. A 10 (2022) 2412–2420.

[12] L. Fischer, K. Ran, C. Schmidt, K. Neuhaus, S. Baumann, P. Behr, J. Mayer, H.J. M. Bouwmeester, A. Nijmeijer, O. Guillon, et al., Role of Fe/Co ratio in dual phase $Ce_{0.8}Gd_{0.2}O_{2-}$ -$Fe_{3-x}Co_xO_4$ composites for oxygen separation, Membranes. 13 (2023).

[13] L. Fischer, K. Ran, C. Schmidt, K. Neuhaus, S. Baumann, P. Behr, J. Mayer, H. J. Bouwmeester, A. Nijmeijer, O. Guillon, et al., Lanthanide element variation in rare earth doped ceria – $FeCo_2O_4$ dual phase oxygen transport membranes, Open Cer. 17 (2024) 100519.

[14] F. Zeng, J. Malzbender, S. Baumann, M. Krüger, L. Winnubst, O. Guillon, W. A. Meulenberg, Phase and microstructural characterizations for $Ce_{0.8}Gd_{0.2}O_{2-\delta}$ -FeCo $_2O_4$ dual phase oxygen transport membranes, J. Eur. Ceram. Soc. 40 (2020) 5646–5652.

[15] F. Zeng, J. Malzbender, S. Baumann, W. Zhou, M. Ziegner, A. Nijmeijer, O. Guillon, R. Schwaiger, W. Albert Meulenberg, Mechanical reliability of $Ce_{0.8}Gd_{0.2}O_{2-\delta}$ -FeCo $_2O_4$ dual phase membranes synthesized by one-step solid-state reaction, J. Am. Ceram. Soc. 104 (2021) 1814–1830.

[16] M. Ramasamy, Dual Phase Oxygen Transport Membrane For Efficient Oxyfuel Combustion, Forschungszentrum Jülich GmbH, 2016.

[17] F. Zeng, J. Malzbender, S. Baumann, A. Nijmeijer, L. Winnubst, M. Ziegner, O. Guillon, R. Schwaiger, W.A. Meulenberg, Optimization of sintering conditions for improved microstructural and mechanical properties of dense $Ce_{0.8}Gd_{0.2}O_{2-\delta}$ -$FeCo_2O_4$oxygen transport membranes, J. Eur. Ceram. Soc. 41 (2021) 509–516.

[18] Picture thresholding using an iterative selection method, IEEE Trans. Syst., Man, Cybern. 8 (1978) 630–632.

[19] A. Kovács, R. Schierholz, K. Tillmann, FEI Titan G2 80-200 CREWLEY, JLSRF 2 (2016).

[20] M. Ramasamy, E.S. Persoon, S. Baumann, M. Schroeder, F. Schulze-Küppers, D. Görtz, R. Bhave, M. Bram, W.A. Meulenberg, Structural and chemical stability of high performance $Ce_{0.8}Gd_{0.2}O_{2-\delta}$ -$FeCo_2O_4$ dual phase oxygen transport membranes, J. Memb. Sci. 544 (2017) 278–286.

[21] F. Zeng, J. Malzbender, S. Baumann, M. Krüger, L. Winnubst, O. Guillon, W. A. Meulenberg, Phase and microstructural characterizations for $Ce_{0.8}Gd_{0.2}O_{2-}$

$_{\delta}$-$FeCo_2O_4$ dual phase oxygen transport membranes, J. Eur. Ceram. Soc. 40 (2020) 5646–5652.

[22] F. Zeng, S. Baumann, J. Malzbender, A. Nijmeijer, L. Winnubst, O. Guillon, R. Schwaiger, W.A. Meulenberg, Enhancing oxygen permeation of solid-state reactive sintered $Ce_{0.8}Gd_{0.2}O_2$-$FeCo_2O_4$ composite by optimizing the powder preparation method, J. Memb. Sci. 628 (2021) 119248.

[23] J. MAIER, Defect chemistry at interfaces, Solid. State Ion. 70-71 (1994) 43–51.

[24] T. Ohnishi, K. Shibuya, T. Yamamoto, M. Lippmaa, Defects and transport in complex oxide thin films, J. Appl. Phys. 103 (2008) 103703.

[25] S. Li, J.T. Irvine, Non-stoichiometry, structure and properties of proton-conducting perovskite oxides, Solid. State Ion. 361 (2021) 115571.

[26] B. Steele, Appraisal of $Ce_{1-y}Gd_yO_{2-y/2}$ electrolytes for IT-SOFC operation at 500°C, Solid. State Ion. 129 (2000) 95–110.

[27] V.V. Kharton, F.M. Figueiredo, L. Navarro, E.N. Naumovich, A.V. Kovalevsky, A. A. Yaremchenko, A.P. Viskup, A. Carneiro, F.M.B. Marques, J.R. Frade, Ceria-based materials for solid oxide fuel cells, J. Mater. Sci. 36 (2001) 1105–1117.

[28] Y. Lin, S. Fang, D. Su, K.S. Brinkman, F. Chen, Enhancing grain boundary ionic conductivity in mixed ionic-electronic conductors, Nat. Commun. 6 (2015) 6824.

[29] W.J. Bowman, J. Zhu, R. Sharma, P.A. Crozier, Electrical conductivity and grain boundary composition of Gd-doped and Gd/Pr co-doped ceria, Solid. State Ion. 272 (2015) 9–17.

[30] W. Lee, H.J. Jung, M.H. Lee, Y.B. Kim, J.S. Park, R. Sinclair, F.B. Prinz, Oxygen surface exchange at grain boundaries of oxide ion conductors, Adv. Funct. Mater. 22 (2012) 965–971.

[31] K. Ran, L. Fischer, S. Baumann, W.A. Meulenberg, K. Neuhaus, J. Mayer, Tuning the ceria interfaces inside the dual phase oxygen transport membranes, Acta Mater. 226 (2022) 117603.

[32] Y. Lei, Y. Ito, N.D. Browning, T.J. Mazanec, Segregation effects at grain boundaries in fluorite-structured ceramics, J. Am. Ceram. Soc. 85 (2002) 2359–2363.

[33] M.B. Mogensen, M. Chen, H.L. Frandsen, C. Graves, J.B. Hansen, K.V. Hansen, A. Hauch, T. Jacobsen, S.H. Jensen, T.L. Skafte, et al., Reversible solid-oxide cells for clean and sustainable energy, Clean Energy 3 (2019) 175–201.

[34] P. Moçoteguy, A. Brisse, A review and comprehensive analysis of degradation mechanisms of solid oxide electrolysis cells, Int. J. Hydrogen. Energy 38 (2013) 15887–15902.

[35] S.P. Jiang, Development of lanthanum strontium manganite perovskite cathode materials of solid oxide fuel cells: a review, J. Mater. Sci. 43 (2008) 6799–6833.

[36] V. Buscaglia, Growth of ternary oxides in the Gd2O3–Fe2O3 system. A diffusion couple study, Solid State Ionics 146 (2002) 257–271.